Tellus (2000), 52A, 473–486
Printed in UK. All rights reserved

TELLUS
ISSN 0280–6495

Strongly stratified easterly flows across Spitsbergen

By PAUL SKEIE* and SIGBJØRN GRØNÅS, *Geophysical Institute, University of Bergen, N-5007 Bergen, Norway*

(Manuscript received 30 March 1999; in final form 31 January 2000)

ABSTRACT

Strongly stratified easterly flow across the Svalbard archipelago is investigated by means of a numerical model with a grid distance of 10 km. Idealized simulations of flow over idealized and real orography with Brunt–Väisälä frequency fixed at $N = 0.019\ s^{-1}$ and with a uniform background velocity varying between 8.7 and 26 ms^{-1} are performed. With a maximum height of the orography at 916 m, the non-dimensional mountain height $\hat{h} = Nh/U$ varies between 0.67 and 2.0. The Rossby number $Ro = U/fL$ is of order unity. Robust features of these simulations are an upstream velocity minimum south of Hinlopenstretet and a downstream wake to the north of Isfjorden. Over the downslopes, upstream of the wake, the velocities are high in the simulations at the lower end of $\hat{h}$ due to vigorous gravity wave activity. As $\hat{h}$ is increased towards 2.0, the gravity wave activity in this area is greatly reduced, and the associated velocity maximum disappears. Downstream jets are radiating from the three resolved fjords Isfjorden, van Mijenfjorden and Hornsund, and the two former jets merge into one further downstream. The absolute velocity maximas are found in the south, where the velocities are enhanced relative to the upstream undisturbed velocity by factors of 1.7 to 2.2. The highest velocities are recognized to be associated with the gravity wave activity. However, velocities are generally high in the south due to the left–right asymmetry induced by planetary rotation. The simulation of a real case largely confirms these findings. In this case wind speeds reaching between 35 and 40 ms^{-1} are simulated near the southern tip of Spitsbergen. An investigation of the zonal wind speeds at Spitsbergen is also presented and reveals that from 1990 to 1997, 13 situations with upstream wind speed of the same strength as in the case study have occurred.

1. Introduction

The winter climatological wind direction at the Svalbard archipelago, located between 76 and 81°N and between 10 and 28°E, is easterly. At this direction, the upstream conditions are dominated by low-level inversions due to a net radiative loss of energy from the sea ice during the polar night. Over the sea ice the arctic inversion is strong and deep (> 1000 m) most days in winter (Serreze et al., 1992). Strong stratification makes flows across Svalbard highly non-linear for most upstream wind speeds. A measure of the non-linearity is provided by the non-dimensional mountain height $\hat{h} = Nh/U$ (the inverse Froude number), where h is the mountain height, U is the background velocity and N is the Brunt–Väisälä frequency. The blocking tendency of an obstacle is enhanced with increasing $\hat{h}$. The highest peak on Spitsbergen, the main island in the group, is 1717 m. A map of the archipelago with smoothed topography is given in Fig. 1. An inversion is characterised by temperature increasing with height. This means that the stability in an isothermal atmosphere forms the lower boundary of the stability in an inversion. The stability in an isothermal atmosphere in terms of the Brunt–Väisälä frequency (N) is $N = 0.0187\ s^{-1}$ at 0°C. A typical tropospheric value of the Brunt–Väisälä frequency at

* Corresponding author.
e-mail: Paul.Skeie@gfi.uib.no

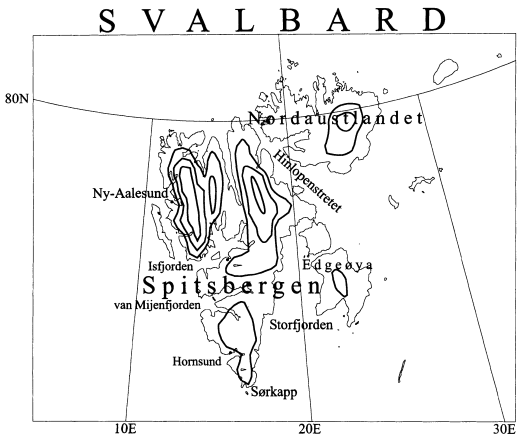

Fig. 1. Map over the Svalbard archipelago with model topography as computed from the 5′ resolution data set. Contours at 400, 600 and 800 m are shown.

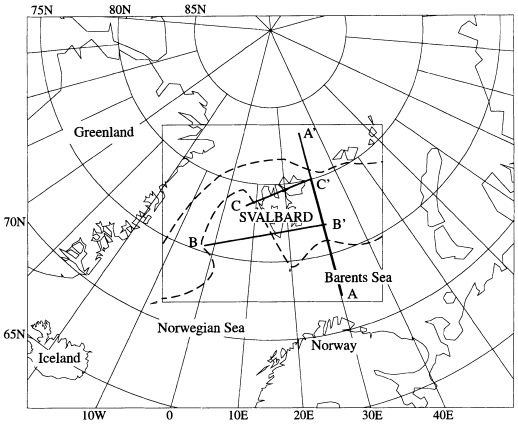

Fig. 2. The model domain used in idealised and real case simulations covers the inner box. Cross-sections mentioned in the text are indicated and labeled AA′, BB′ and CC′. The dashed lines indicates climatological sea ice limits in late winter and late summer (Hanssen-Bauer et al., 1990).

mid-latitudes is $N = 0.01\ \mathrm{s}^{-1}$. This means that non-linearities for flows across Spitsbergen are comparable to the non-linearities in flows across far higher orography elsewhere in the world, e.g., the Central European Alps. The synoptic scale climate at Spitsbergen is dominated by the arctic high to the north and extratropical cyclone tracks over the Norwegian and Barents Seas to the south (Jones, 1987; Overland and Pease, 1982; Serreze et al., 1993). The climate of Spitsbergen is strongly moderated by open waters to the west due to the West Spitsbergen Current, an extension of the North Atlantic Current. Annual maximum and minimum sea ice limits are shown in Fig. 2. Strong easterly airflows occur when extratropical cyclones passes south of Spitsbergen, as they make their way into the Barents Sea.

The airflow over Spitsbergen is important to document, not only for the obvious purpose of weather forecasting. With its location at the brim of the arctic ice sheet, the air–sea interaction in the area is vigorous due to large air to sea temperature differences. The formation of sea ice leads to brine rejection, and plumes of dense water have been observed in Storfjorden between Edgeøya and Spitsbergen (Quadfasel et al., 1988). This mechanism is expected to play a central role in the renewal of the deep waters of the Arctic Mediterranean, a key factor in the large scale thermohaline circulation.

Numerical models have proved invaluable in studies of flow across complex terrain. In this work the Norwegian hydrostatic model NORLAM has been applied with 10 km grid distance. The use of a hydrostatic model is considered justifiable since the highest frequency imposed onto the flow at this resolution is $U_{\max}/2\Delta x \approx 0.001\ \mathrm{s}^{-1}$, which is one order of magnitude smaller than typical tropospheric values of the Brunt–Väisälä frequency. Considering the ability of mesoscale models to simulate observed flow features, we feel confident that real insight in flow over Spitsbergen is gained from these simulations. In this work the model has been used in idealised simulations with idealised and real topography and in the simulation of a real case.

Section 2 contains theoretical considerations and references to relevant theory. The numerical model is described briefly in Section 3 together with information about the applied datasets. Results from the idealised runs are given in Section 4. Results from the real case along with an observational context are given in Section 5 and finally, discussions are contained in Section 6.

2. Theory

According to Smith (1989a), there are three regimes in upstream barotropic flows over simple

3-D mountains. If the non-dimensional mountain height is small, no stagnation points are observed and the flow is characterised by some deflection of the flow around the mountain and gravity waves. The other two regimes are connected to stagnation points, either on the lower boundary of the windward slope, or at the first steepening level of the streamlines above the lee slope, where the negative perturbation in the horizontal velocity has its maximum. For long ridges oriented perpendicular to the flow, the tendency for stagnation above the lee slope is far stronger than at the windward slope, while for mountains with a circular shape, the stagnation might, according to linear theory, occur equally frequent at both points (Smith, 1989a).

Windward stagnation allows flow splitting, i.e., the left–right splitting of the low-level centre streamline. This idea has been studied in a non-hydrostatic numerical model by Smolarkiewicz and Rotunno (1989). They found that the formation of stagnation points is also connected to a wake structure behind the obstacle. The simulations of Smolarkiewicz and Rotunno (1989) showed that two counter-rotating vortices like those observed behind Hawaii could occur without involving any surface friction. Smolarkiewicz and Rotunno (1989) suggested that vorticity is produced baroclinically through tilting of the isentropes. Later, it has been pointed out by Schär and Smith (1993) that vorticity may be produced by dissipation when the flow goes through a hydraulic jump.

For idealised unrotational flows across a circular Gaussian mountain, Smith and Grønås (1993) found that stagnation first occurs in the lee. The critical height was found to be 1.1 ± 0.1. The presence of positive vertical wind shear suppresses stagnation aloft, while negative vertical wind shear enhances the tendency for stagnation (Smith, 1989a). Stagnation above the lee slope may trigger severe down-slope winds. Peltier and Clark (1979) found that when a critical value of the non-dimensional height $\hat{h} = hN/U$ is exceeded, a turbulent structure appears and the flow begins to evolve in time and eventually reaches a new steady state with severe lee winds. In this state, the wave breaking de-couples the flow below from the flow above the breaking region. This allows the flow below to be described by a local hydraulic theory (Smith, 1985).

A simple approach to strong lee winds and hydraulic jumps can be gained from the non-linear shallow water equations (e.g., Pedlosky, 1979):

$$\frac{\mathrm{D}\boldsymbol{v}}{\mathrm{D}t} + g^*\nabla(H+h) = 0, \tag{1}$$

$$\frac{\partial H}{\partial t} + \nabla\cdot(H\boldsymbol{v}) = 0, \tag{2}$$

where

$$\frac{\mathrm{D}}{\mathrm{D}t} = \frac{\partial}{\partial t} + u\frac{\partial}{\partial x} + v\frac{\partial}{\partial y} \tag{3}$$

is the total derivative operator, $\boldsymbol{v}$ is the horizontal velocity vector with components (u, v), H is the layer thickness, h is the topography, and $g^* = g(\delta\theta/\theta)$ is the reduced gravity with g, θ and $\delta\theta$ referring to the acceleration of gravity, potential temperature and the potential temperature difference between the upper and lower layer. The linearised steady state solution of these equations for flow over a mountain, depends on the Froude number. This is defined $F = U^2/c^2$ where U is the velocity and $c^2 = g^*H$ is the phase speed of the shallow water gravity waves. When F is larger than unity, horizontal velocity is larger than the propagation speed of the gravity waves and the upstream propagating mode is swept downstream, disabled to influence the steady state solution. In the supercritical (subcritical) regime, the layer thickness H has a maximum (minimum) over the mountain, whereas the velocity has a minimum (maximum) which means that the acceleration zone in the subcritical regime is upstream of the mountain while it is downstream in the supercritical regime. In highly non-linear subcritical flows, upstream acceleration and reduction of H might make F larger than unity (and the flow supercritical) locally, implying acceleration both upstream and downstream of the mountain. This provides an explanation of strong lee winds. The abrupt transition back to the subcritical regime is referred to in the literature as a hydraulic jump.

The horizontal scale of Spitsbergen is sufficiently large that the Coriolis force has a significant influence on the perturbations. An important effect of rotation and the presence of a large scale pressure gradient is caused by the retarding effect on the flow of the positive pressure perturbation that is generated upstream of the mountain by adiabatic ascent. As the air rises to climb the

mountain, it cools adiabatically and a positive pressure perturbation is formed below. Air in geostrophic balance entering this positive pressure perturbation is retarded, and feeling a weaker Coriolis force it starts accelerating towards low pressure in the synoptic system. On the northern hemisphere the air will be accelerated on the left side of the mountain. As the air ends up at lower pressure, a Bernoulli consideration implies an increase in the kinetic energy. Furthermore, the Coriolis force acts on the cross-flow perturbations and accelerates the flow that is deflected to the left of the mountain in the direction of the incident flow. The flow will consequently be shifted to the left of the mountain facing downstream.

3. The numerical model and data sets

For this study, the Norwegian limited area model (NORLAM) has been used. It is described in Grønås and Hellevik (1982), Nordeng (1986) and Grønås (1987). It is a hydrostatic model written in σ-coordinates on a stereographic map. In these runs 30 layers have been used with the top layer at 100 hPa. The layers are evenly distributed in pressure. An absorbing layer, with diffusion increasing with height, prevents reflection from the top boundary. The surface-layer parameterisation follows Louis (1979). Turbulence is parameterized with a K-exchange coefficient scheme, activated whenever the bulk Richardson number drops below 0.5. The radiation-, cloud- and precipitation schemes are according to Nordeng (1986). Horizontal diffusion is used at the top layers only. A second order Shapiro filter (Haltiner and Williams, 1980) is used every hour to remove small-scale energy. The lateral boundary values are updated every 6 h using the relaxation method of Davies (1976) on the first 6 lateral grid points of the domain.

The Spitsbergen orography which is shown in Fig. 1 is computed from a 5′ resolution data set obtained from the U.S. Geologic Survey. The maximum height of the model orography is 916 m. In the case study, the model is initialised with analyses of upper air fields from the European Centre for Medium range Weather Forecasting (ECMWF). The ice and sea surface temperature (SST) data used in the case study are provided by Det Norske Meteorologiske Institutt (DNMI). Daily northern hemisphere sea level pressure (SLP) data on a $5^\circ \times 5^\circ$ grid from NCAR is used to analyse the zonal geostrophic wind climatology of Spitsbergen.

4. Idealised simulations

This section contains results from numerical simulations of easterly flow over Spitsbergen with controlled upstream conditions. The NORLAM model, with physics included, is used in these simulations as well as in the case study. However, in the idealised experiments the mapping factor and the Coriolis parameter are invariant on the grid and the sensible heat flux from the ground has been switched off to keep the vertical stability unaltered throughout the simulations. The roughness length is set to 0.001 m over ice covered areas and 0.3 m over land. In the idealised runs the entire domain is covered with ice. However, in one experiment an ice-cover identical to that of the real case has been used, and in this experiment the sensible heat flux is switched on. All the idealised simulations are initialised with uniform wind, Brunt–Väisälä frequency and temperature horizontally and vertically and the boundaries are held constant during the simulations. The standard definition of the Brunt–Väisälä frequency is

$$N^2 \equiv \frac{g}{\theta}\frac{\partial \theta}{\partial z}, \tag{4}$$

where g is the acceleration of gravity and θ is the potential temperature. The isothermal Brunt–Väisälä frequency is more easily found from the definition

$$N^2 = \frac{g}{T}\left[\frac{\partial T}{\partial z} + \frac{g}{c_\mathrm{p}}\right] \tag{5}$$

that may be derived by combining eq. (4) with the Poisson equation. In an isothermal atmosphere the first term inside the brackets of eq. (5) vanishes and the Brunt–Väisälä frequency is simply

$$N^2 = \frac{g^2}{c_\mathrm{p} T}. \tag{6}$$

In the idealised simulations the Brunt–Väisälä frequency is set to $N = 0.019\ \mathrm{s}^{-1}$, corresponding to a temperature of $T = 265.5$ K. The strong stratification in these idealised runs is presumed realistic for easterly flow over Spitsbergen where inver-

sions frequently occur. However, it should be emphasised that even though the isothermal Brunt–Väisälä frequency is large compared to typical values in the troposphere, it is at the lower end of inversion Brunt–Väisälä frequencies.

The initial flow is geostrophically balanced and directed along the negative x-axis of the grid. The height of the pressure surfaces is given by

$$z = -\frac{\kappa g}{N^2} \ln\left(\frac{p}{p_s}\right), \tag{7}$$

and the pressure gradient is calculated by integrating the geostrophical balance equation $\partial p/\partial y = -f_0 \rho U$ on the surface combined with the ideal gas equation to yield

$$p_s(y) = p_s(y_0) \exp\left[-\frac{f_0 U}{RT}(y - y_0)\right], \tag{8}$$

where $p_s(y_0)$ is the surface pressure on the southern boundary. All the simulations are run for at least $tU/L = 30$ normalised time units (τ), where t is the time (s) and L is a typical horizontal length scale of the topography. The idealised simulations are summarised in Table 1.

4.1. *Flow over an idealised mountain*

The experiments exp1 through exp5 are conducted with an idealised circular "Witch of Agnesi" shaped mountain defined by

$$H(x, y) = \frac{ha^2}{x^2 + y^2 + a^2}, \tag{9}$$

where $h = 916$ m is the height and $a = 50$ km is the horizontal scale of the mountain represented by the half-width. The height of this idealised mountain is the same as the maximum height of the real topography of the other experiments. In all the simulations of flow across this circular mountain, a wake is formed. However, the wake characteristics are quite different for the different values of $\hat{h}$ used. In exp5, where $\hat{h} = 0.67$, the wake is confined to an area just downwind of the mountain, while the wake in exp4 is long and straight. The wake flow is relatively unidirectional for the simulations with $\hat{h} \leqslant 1.34$, while vortex shedding occurs when $\hat{h}$ is 1.75 and 2.0. Upstream return flow at the surface is present in exp1, exp2 and exp3 where $\hat{h} \geqslant 1.34$, which concords with results reported by Smith and Grønås (1993) without rotation or friction. Fig. 3 shows the flow at $\sigma = 0.988$ in exp3 at $\tau = 22$ (24 h). After this time there are no important changes in the flow. The Rossby number is 1.9 and the effect of planetary rotation and the presence of a large-scale pressure gradient is manifested through the left–right asymmetry of the flow. The upstream low velocity area is shifted to the right-hand side of the mountain, while the downstream high velocity area is shifted to the left. The maximum velocity (U_{max}) is more than 22 ms^{-1}, which is 1.7× the undisturbed upstream velocity (U). This is the same for all the simulations exp1 through exp4 (Table 1). Similar stabilities in this ratio have been reported by Olafsson and Bougeault (1996). For exp5, where $\hat{h} = 0.67$, the ratio U_{max}/U is 1.5, which shows that this run is closer to the linear regime, although the magnitude of the perturbations are still 50% of the background flow.

There is no return flow at the first steepening

Table 1. *Overview of the idealised simulations*

Experiment	Topography	N	U	$\hat{h}$	Ro	Ice cover	U_{max}/U
exp1	eq. (9)	0.019 s^{-1}	8.7 ms^{-1}	2.0	1.3	total	1.7
exp2	eq. (9)	0.019 s^{-1}	10 ms^{-1}	1.75	1.5	total	1.7
exp3	eq. (9)	0.019 s^{-1}	13 ms^{-1}	1.34	1.9	total	1.7
exp4	eq. (9)	0.019 s^{-1}	19 ms^{-1}	0.92	2.8	total	1.7
exp5	eq. (9)	0.019 s^{-1}	26 ms^{-1}	0.67	3.7	total	1.5
exp6	real	0.019 s^{-1}	8.7 ms^{-1}	2.0	1.3	total	2.1
exp7	real	0.019 s^{-1}	10 ms^{-1}	1.75	1.5	total	2.1
exp8	real	0.019 s^{-1}	13 ms^{-1}	1.34	1.9	as Case 1	2.1
exp9	real	0.019 s^{-1}	13 ms^{-1}	1.34	1.9	total	2.2
exp10	real	0.019 s^{-1}	19 ms^{-1}	0.92	2.8	total	2.0
exp11	real	0.019 s^{-1}	26 ms^{-1}	0.67	3.7	total	1.7

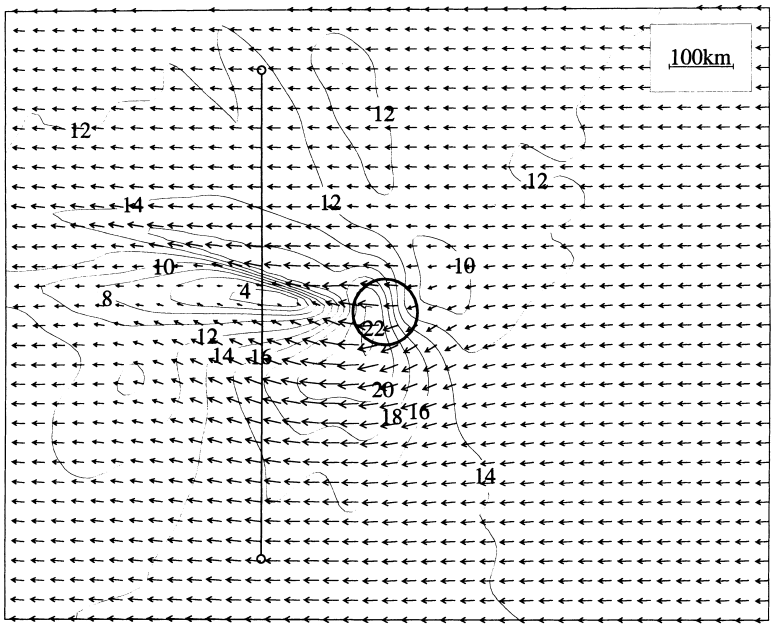

Fig. 3. Low-level flow represented by wind arrows and isotachs at $\sigma = 0.988$ after 24 h of simulation in exp3. The position of the mountain is indicated by a contour at $h/2 = 458$ m. The line through the wake indicates the position of the cross-section shown in Fig. 14.

level of the isentropes above the downwind slope in any of the simulations exp1 through exp5. The vertical wavelength of the gravity waves shows good agreement with the vertical hydrostatic wavelength $\lambda_z = 2\pi U/N$ deduced from linear theory of 2-dimensional gravity waves. In exp3 linear theory predicts a vertical wavelength of $\lambda_z \approx 4300$ m. By visual inspection of Fig. 4, the centre of the low velocity area around the first steepening level above the lee slope is at approximately 800 hPa. Solving for p in Eq. (7) and using $p_s = 800$ hPa, the centre of the next low velocity area (one wavelength above) should be at 460 hPa which is in good agreement with Fig. 4. Due to horizontal dispersion, the wave amplitude decays with height.

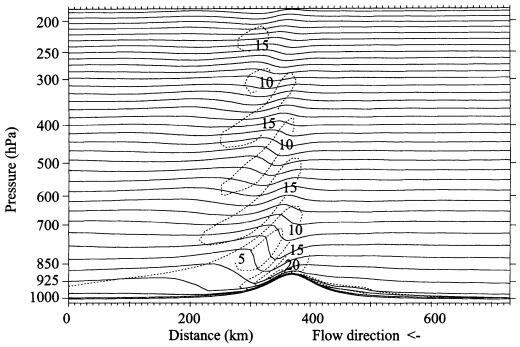

Fig. 4. Vertical cross-section parallel to the incident flow along the centerline of the idealised mountain in exp3 after 24 h of simulation. Isentropes are drawn with solid lines for every 5 K. The velocity contours are dashed.

4.2. *Idealised flow over real topography*

All the runs exp6 through exp11 are subcritical with respect to the highest mountains, and many general features of the simulated flows show a large degree of similarity. To facilitate the discussion of these common features, a snapshot of the low-level flow after 24 h of simulation in exp9 is shown in Fig. 5. The non-dimensional mountain height in this run, calculated by using $h = h_{max}$, is 1.34. In all runs exp6 through exp11 the lowest upstream velocities are found south of Hinlopenstretet between Nordaustlandet and Spitsbergen (see Fig. 1 for the location). Hinlopenstretet is just upstream of the highest mountains on Spitsbergen. The upstream min-

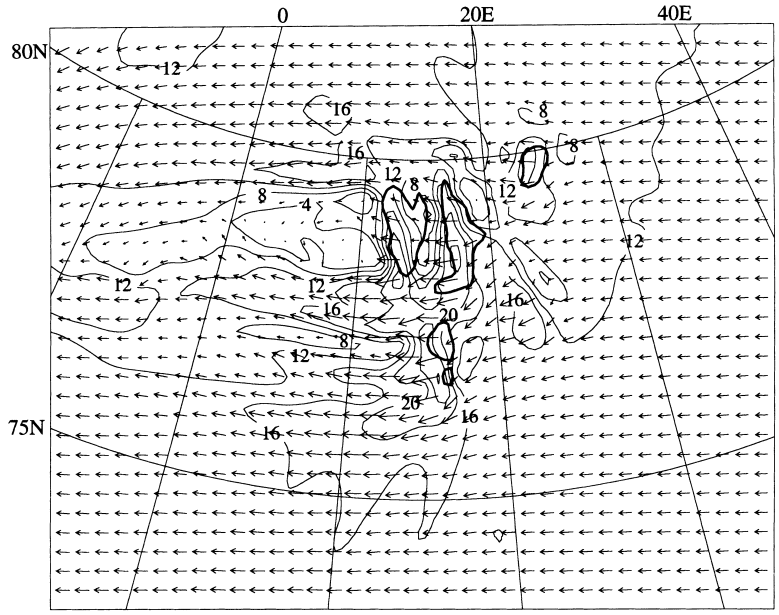

Fig. 5. Low-level flow represented by wind arrows and isotachs at $\sigma = 0.988$ after 24 h of simulation in exp9. The position of the main mountains is indicated by contours at $h_{max}/2 = 458$ m.

imum velocity area is clearly shifted to the right of the 458 m contour, as well as to the right with respect to the total land mass of the archipelago. There is a pronounced tendency for the air to be diverted southwards all over the upstream influence zone and only in the far north, northwards perturbations are found. These perturbations form a jet from the northern tip of Spitsbergen. To the south of the low velocity area, the southwards diverted air contributes to the jets that radiate out of Isfjorden and van Mijenfjorden and merge into a broader jet further downstream. The wake downstream of the highest mountains is linked to the blocking and bifurcation of the flow south of Hinlopenstretet. In the runs with $\hat{h} = 1.34$ and lower, high velocities are found near the downwind slopes. The transition to wake conditions is abrupt and linked to steeply rising isentropes (Fig. 6). This transition might be characterised as a hydraulic jump. In the runs where $\hat{h}$ is larger than 1.34, the velocities on the downslope, upstream of the wake, are not enhanced similarly to the runs with $\hat{h} = 1.34$ and lower. In these runs there is only a weak flow across the ridge upstream of the wake, i.e., the blocking is almost complete and the gravity waves are weak.

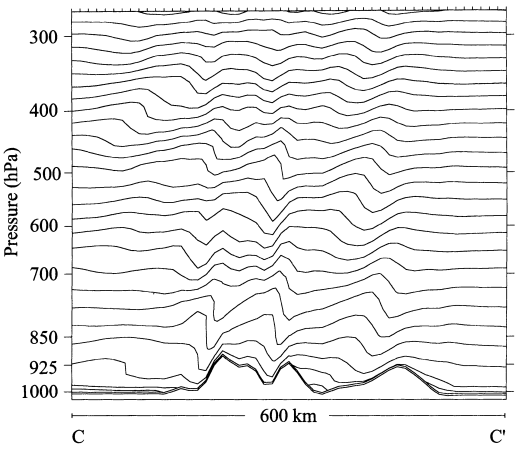

Fig. 6. Cross-section CC′ in Fig. 2 showing isentropes after 24 h of simulation in exp9. The equidistance is 5 K.

For the same values of $\hat{h}$, blocking in the runs with realistic topography is far more pronounced than in the runs with an idealised circular mountain (compare exp9 in Fig. 5 with exp3 in Fig. 3). There are also clear differences in the wake characteristics. The wake flow in exp9 is highly disorganised and variable in time in contrast to exp3,

where the wake flow is quite unidirectional and stationary. In this respect, the wake in exp9 shows closer resemblances with the wakes in higher $\hat{h}$ flows over the idealised mountain. This is in accordance with Smith (1989b), who investigated stagnation for a family of ellipsoidal hills. He found that both upstream stagnation and stagnation over the lee slope occurs for a lower $\hat{h}$ for ridges oriented in a cross-flow direction, than for circular mountains.

The highest velocities in the runs with real topography are found near the downwind slopes of the mountains between van Mijenfjorden and Sørkapp, where the undisturbed upstream velocity is more than doubled. These high velocities are associated with a gravity wave aloft. A cross-section through the wave is shown in Fig. 7. The isentropes are steep and close to overturning. The mountains between van Mijenfjorden and Sørkapp, which in the model topography has a maximum height of 585 m, shows an increasing tendency to block the flow with increasing values of $\hat{h}$. The narrow downwind wake that may be identified to the south of the jet out of van Mijenfjorden and to the north of the jet out of Hornsund in Fig. 5, has in exp7 increased in cross-flow width. In this simulation as well as in exp6 a wake is formed which is bounded by the van Mijenfjorden jet in the north and the Sørkapp jet in the south. This wake is only partly penetrated by the Hornsund jet.

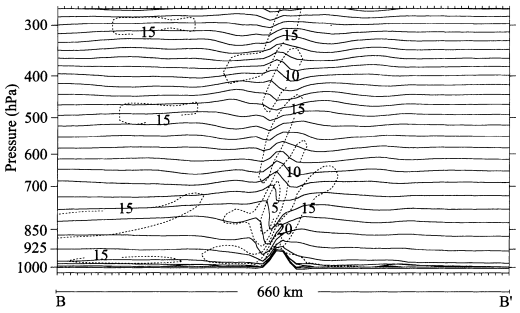

Fig. 7. Cross-section BB′ of Fig. 2 in exp9 after 24 h of simulation. Isentropes are drawn with solid lines for every 5 K. The velocity is dashed.

5. A real case

In this section, results from a real case will be shown. First the upstream geostrophical wind speed in this case will be put into an observational context. A climatology of zonal airflows over Spitsbergen can be estimated from the NCAR SLP dataset with $5^\circ \times 5^\circ$ resolution for the period 1940 to 1996. The observations were made at 12 UTC up to April 1956 and from there and onwards at both 00 and 12 UTC. By using the geostrophic balance equation $u_g = -(\Delta p/\rho f \Delta y)$, with density $\rho = 1.28\ \mathrm{kgm}^{-3}$ and Coriolis parameter $f = 1.42 \cdot 10^{-4}\ \mathrm{s}^{-1}$, the mean zonal geostrophic wind u_g between two grid points at 80°N 30°E and 75°N 30°E may be calculated. The deduced u_g for January only, has been sorted into $5\ \mathrm{ms}^{-1}$ bins and the relative frequency of each bin is given in Table 2. 62.6% of the deduced January zonal winds are easterly and 23.4% are easterly with velocities above $10\ \mathrm{ms}^{-1}$. Considering all calendar months, easterly winds in excess of $25\ \mathrm{ms}^{-1}$ were observed 17 times prior to 1990. In the much shorter period 1990 to 1996, easterly winds of this strength have been observed 21 times distributed on 13 separate events, which is almost 2 episodes a year. Deduced winds exceeding $30\ \mathrm{ms}^{-1}$ are only observed 3×, all of which are in the nineties. This indicates a tendency towards more extreme cases during the 90s compared to the period 1940–1989.

For the particular case that will be studied here, the upstream geostrophic wind speed deduced from NCAR SLP data between 80°N 30°E and 75°N 30°E is given in Table 3. The upstream wind is strong, but as mentioned above, 13 situations with winds of equal strength have occurred during the first seven years of the nineties. The distribution of sea ice and SST in the model domain, is shown in Fig. 8. The ocean north and east of

Table 2. *Frequency distribution of zonal geostrophic wind in January between 80°N 30°E and 75°N 30°E from 1940 to 1996; the data has been sorted into 5 ms^{-1} bins*

bin centre (ms^{-1})	−27.5	−22.5	−17.5	−12.5	−7.5	−2.5	2.5	7.5	12.5	17.5	22.5
frequency (%)	0.1	1.9	6.2	14.9	22.9	24.7	16.2	8.3	3.5	0.8	0.1

Table 3. *Temporal development of upstream geostrophic wind from 24 January 00 UTC deduced from pressure difference between 80°N 30°E and 75°N 30°E from NCAR SLP data*

hours	+00 h	+12 h	+24 h	+36 h
zonal velocity	21.4 ms^{-1}	26.4 ms^{-1}	28.6 ms^{-1}	26.5 ms^{-1}

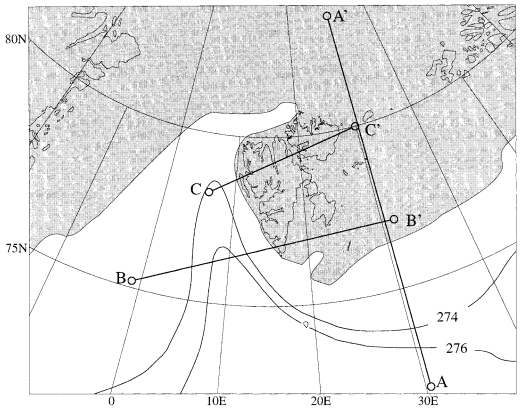

Fig. 8. Ice cover and sea surface temperature (SST) for 24 January 1995. SST is in Kelvin and only two isotherms are drawn. The shaded grey area is covered with ice. The analyses are provided by the DNMI. Cross-sections mentioned in the text are drawn as lines and labeled AA′, BB′ and CC′.

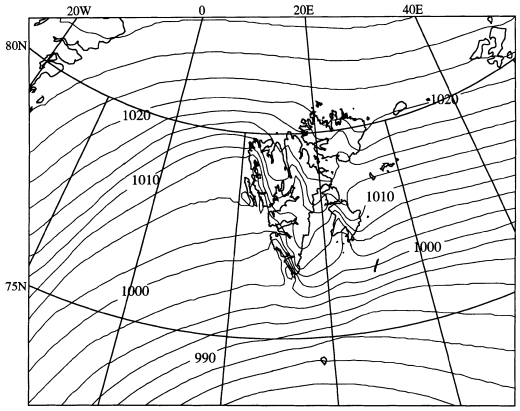

Fig. 9. Simulated mean sea level pressure at 25 January 00 UTC. The equidistance is 2.5 hPa.

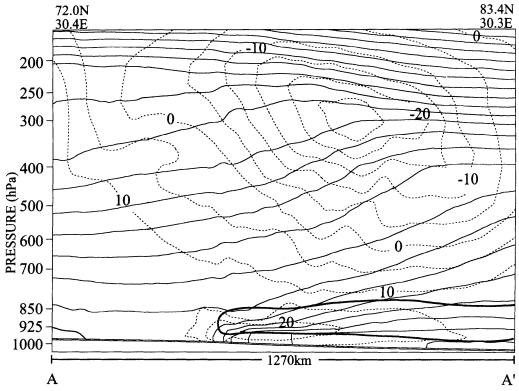

Fig. 10. Cross-section AA′ in Fig. 8 valid at 25 January 00 UTC. Solid lines are isentropes and dashed lines are isotachs for wind normal to the cross-section. The equidistance is 5 ms^{-1} for wind speed and 5 K for potential temperature. The inversion is indicated by a heavy solid line.

Spitsbergen is covered by ice, whereas the ice edge to the west of Spitsbergen almost coincides with the coastline.

The integration is initialised at 00 UTC 24 January, when a slow-moving extratropical low is positioned with centre over central Scandinavia, directing an easterly surface flow over Spitsbergen. The predicted surface pressure valid at 00 UTC the next day is shown in Fig. 9. The easterly flow at 25 January 00 UTC is strong and fairly steady. A cross-section of the upstream conditions of Spitsbergen is found in Fig. 10. The flow is characterised by a marked inversion close to the surface, reaching around 850 hPa. In this inversion the Brunt–Väisälä frequency varies between 0.02 and 0.03 s^{-1}. In Fig. 10, the inversion top is marked where the vertical temperature gradient changes from isothermal to less stable stratification. The inversion height increases northwards to 800 hPa at 80° north. There is a low-level jet with a velocity maximum of 26 ms^{-1} around 925 hPa at the ice edge. Above the inversion, there is a baroclinic structure with relatively warm air over the ocean and cold air over the interior of the ice. The thermal wind induces a backing shear that reduces the wind to zero in the mid-troposphere and beneath the tropopause there is a westerly jet with a velocity of 28 ms^{-1}. Compared to the idealised runs, the stability is larger in the low-level inver-

sion and lower above. The real case also differs from the idealised simulations in that there are surface inhomogeneities in friction and heat fluxes at the ice edge.

The low-level flow after 24 h of integration is shown in Fig. 11. Although the flow at this time is more northerly, it resembles largely what was observed in the idealised simulations with real topography. The most important jets and wakes are present as well as the velocity minimum south of Hinlopenstretet. The reduced stability above the inversion and the backing shear do not seem to change the overall picture dramatically.

The highest velocities are found near Hornsund and at the tip of Sørkapp with values between 35 and 40 ms^{-1}. Fig. 12 shows a cross-section through the gravity wave above Sørkapp. The amplitude of the mountain wave is largest above the inversion. The total wave energy per unit volume, when the x-axis is aligned with the mean flow (Baines, 1995), is:

$$E = \frac{1}{2}\rho_0(u'^2 + w'^2 + N^2\eta^2), \tag{10}$$

where ρ_0 is the mean density, u' and w' are the horizontal and vertical wave perturbation velocities, N is the Brunt–Väisälä frequency and η is the vertical displacement of the streamlines from the horizontal. Eq. (10) shows that the potential energy (the last term) associated with a certain vertical displacement is proportional to N^2. A non-diverging vertical flux of energy with constant energy will consequently require increased displacement in layers with reduced stability in accordance with the wave shown in Fig. 12. However, as pointed out by Eliassen and Palm (1960), in 2-dimensional stationary waves where the mean flow U is varying with height there is an exchange of energy between the waves and the mean flow and the wave energy is generally not constant with height. The exchange of energy in that special case is described by the equation

$$\frac{\mathrm{d}}{\mathrm{d}z}\overline{p'w'} = -\rho_0\frac{\mathrm{d}U}{\mathrm{d}z}\overline{u'w'}, \tag{11}$$

where p' is the wave induced pressure perturbation and the overbar denotes a horizontal integration operator. Eliassen and Palm (1960) identified the vertical flux of energy as $\overline{p'w'}$ and the vertical flux of momentum as $\rho_0\overline{u'w'}$. In this situation, there is a negative velocity shear and since the vertical flux of momentum in a mountain wave is negative

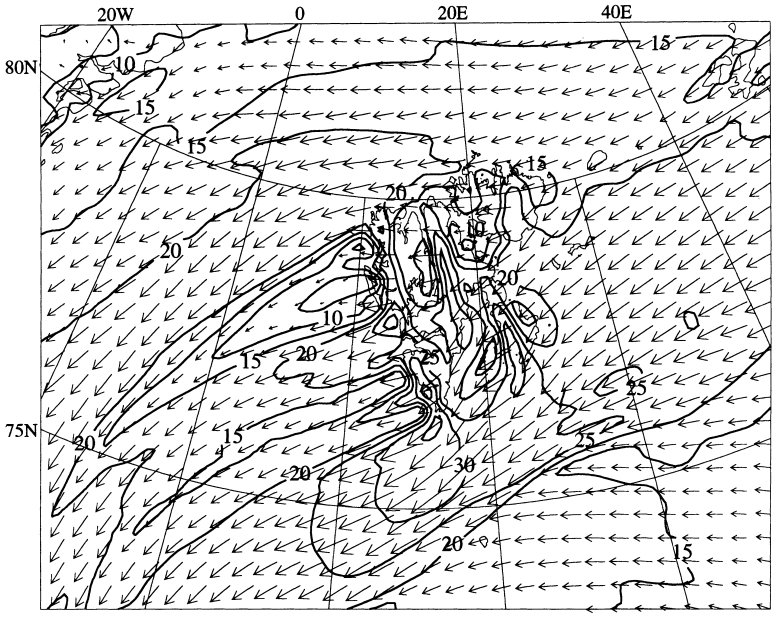

Fig. 11. Low-level flow represented by wind vectors and isotachs in $\sigma = 0.955$ valid at 25 January 00 UTC. The equidistance for wind speed is 5 ms^{-1}.

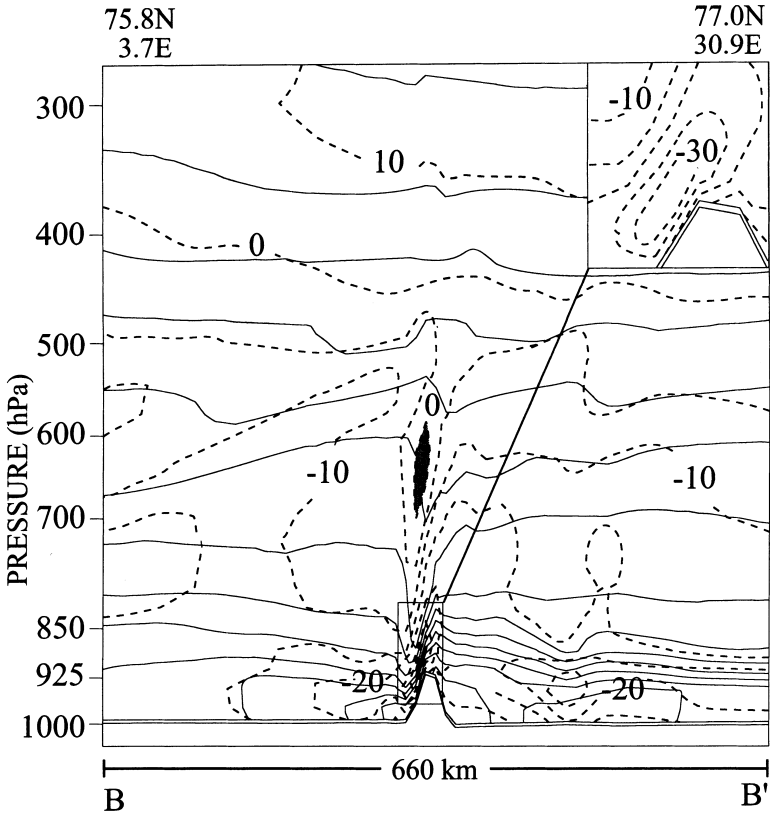

Fig. 12. Cross-section BB′ of Fig. 8, valid at 25 January 00 UTC, showing isentropes (solid) and isotachs (dashed) for the velocity component parallel to the cross-section. The equidistance is 5 ms^{-1} for wind speed and 4 K for potential temperature. The shaded area is indicating return flow with respect to the ambient flow. In the upper right corner is zoomed view of the velocity in the indicated rectangle over the mountain.

(u' and w' is negatively correlated) the right-hand side of eq. (11) is negative, implying that the vertical flux of energy decays with height and energy is being transferred from the waves to the mean flow. Another important result from Eliassen and Palm (1960) is that the vertical flux of momentum is constant with height in 2-dimensional stationary gravity waves, provided that the mean flow is not zero at some level. The 3-dimensionality, the critical layer and the wave breaking clearly violates these simplifying assumptions and the model simulates a divergence in the vertical momentum-flux below the critical layer since the wave signature fades approaching the critical layer from below. This divergence is associated with transfer of momentum from the wave to the mean flow resulting in a retardation of the mean flow. The high amplitude waves simulated in this case do not break in the sense that they are destroyed. This is in agreement with the "saturation hypothesis" formed by Lindzen (1981) which states that the waves only break partially, to the point where dynamical stability is regained. Wave breaking is simulated over Sørkapp and Ny-Ålesund, where the isentropes are close to overturning and patches with return flow are seen. Over Ny-Ålesund jump-like structures (see Section 2) are simulated, with strong winds over the lee slope and an abrupt transition to wake conditions at the coast where the isentropes rises and the flow decelerates (Fig. 13).

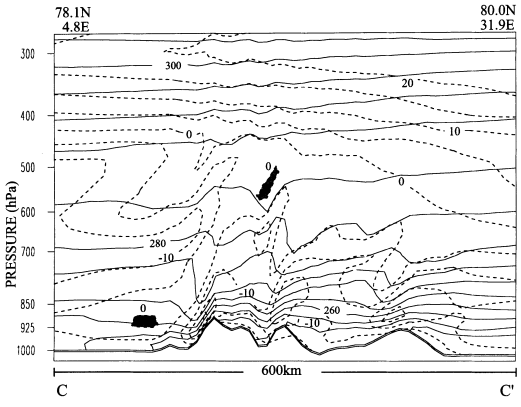

Fig. 13. Cross-section CC′ in Fig. 8 showing isentropes (solid) and parallel component isotachs (dashed) valid at 25 January 00 UTC. The equidistance is 5 ms^{-1} for wind speed and 4 K for potential temperature. The shaded area is indicating return flow with respect to the ambient flow.

6. Discussion

Simulations of flow across an idealised circular mountain represents a somewhat oversimplified approach to easterly flow across the Svalbard archipelago. The most important shortcomings are absence of steep topography, asymmetries, different length scales in along- and across-flow directions and fine scale details. Despite of these shortcomings, valuable information might be gained by looking at differences and similarities between the flows across the idealised and real topography. A variety of spatial scales are present in the real topography, opening for spatial scale interactions that are absent in the idealised topography runs. The effect of the largest scales of the Spitsbergen topography on the flow should show similarities with the flow over the idealised circular mountain. Although direct spatial interactions will take place, one may to the first order regard this low Rossby number flow as a background flow for the flow across finer details in the topography. Following this line of reasoning, the adjusted background flow might vary across the archipelago and different non-dimensional mountain heights $\hat{h}$ might apply for the same actual mountain height h. With the flow shown in Fig. 3 in mind, the impact of a small scale peak on the upstream right, will consequently be different from the impact of the same peak on the downstream left-hand side of the large scale mountain. In Section 4 we showed that for the same value of $\hat{h}$, the blocking tendency of the real topography was more pronounced than that of the idealised circular mountain and this was attributed to the ridge-like structures of the North Spitsbergen topography. We hypothesize that the combined effect of the left–right asymmetry of the topography and the left–right asymmetry due to planetary rotation on flow past an obstacle, might play a role as well since the highest mountains are on the same side as the presumed lowest velocities.

There is a large difference between the maximum height of the real topography and the model topography. Some peaks in the real Svalbard topography penetrates several σ-levels. Drag parameterizations that allows the drag to act directly on the model levels penetrated by subgrid-scale peaks, have been shown to reinforce the low-level wake in better agreement with observations (Lott and Miller, 1997). We therefore expect our simulations to underestimate the blocking and wake formation.

The wake in exp3 is asymmetric with respect to the axis of the incident flow. The cyclonic vertical vorticity component to the right of the wake is much stronger than the anti-cyclonic vorticity to the left. Inertial instability requires that $(f - (\partial u_g/\partial y)) < 0$, and this condition is met on the left side of the wake. Fig. 14 shows that the cyclonic vorticity to the right exceeds the planetary

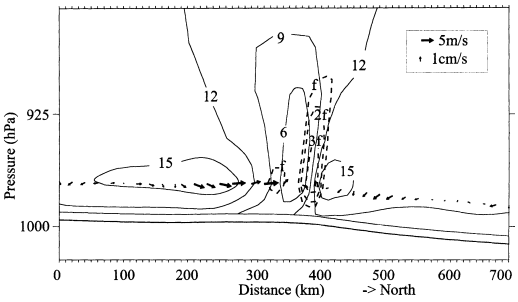

Fig. 14. Vertical cross-section showing velocity and vorticity in the wake after 24 h of simulation in exp3. The position of the cross-section is shown in Fig. 3. The isotachs indicates wind along negative x-axis of the grid. The wind contours are solid, with an equidistance of 3 ms^{-1}. The vorticity is contoured with dashed lines for every $f = 1.4 \cdot 10^{-4}\ s^{-1}$ where f is the Coriolis parameter. The zero contour has been omitted. The ageostrophic and vertical motions at $\sigma = 0.988$ are indicated as arrows.

vorticity (f) with a factor of more than three, while the negative vorticity to the left is around $-f$. This suggests the possibility that inertial instability prevents the relative vorticity from dropping much below $-f$ on the anti-cyclonic side. One may argue as follows: If a parcel of air to the left of the wake, moving along the negative x-axis of the grid, is perturbed towards the wake, the Coriolis force will act to the right of this lateral motion and thereby reduce the velocity-component along the negative x-axis. Under normal atmospheric conditions, the absolute vorticity is positive and this reduction in velocity reduces the Coriolis force sufficiently that the pressure gradient will force the parcel back to its initial y-axis position. However, in situations where a strong anti-cyclonic geostrophic shear is present, a parcel perturbed to the right will enter the wake where the pressure gradients are too weak to force the parcel back to its initial position even though its velocity component along the negative x-axis is reduced by the Coriolis force. This will result in an ageostrophic flow towards the wake that will reduce the velocity component along the negative x-axis and hence, the anti-cyclonic shear. Fig. 14 shows that there is indeed an ageostrophic flow towards the wake in the anti-cyclonic shear zone. With the condition $(f - (\partial u_g/\partial y)) < 0$ clearly met, inertial instability is a likely explanation for this flow. This suggests that inertial instability can play a role in decelerating the flow exterior to the wake core on the left-hand side in flows with Rossby number of order unity. The result will be a left-hand side broadening of the wake.

The strong topographic steering of atmospheric flows across the Svalbard archipelago may be of interest to researchers in the marine sciences. The Svalbard mountains divert the easterly flows southwards, causing northerly winds in the Storfjorden area. The southerly advection of sea ice out of Storfjorden during winter, causes a divergent ice field and a large ice production in the fjord. The brine released to the water column produces an extremely dense water mass (Quadfasel et al., 1988; Schauer, 1995). Another aspect of relevance for air–sea interaction is the strong vorticity in the downstream windfield of Spitsbergen. Curls in the wind stress leads to Ekman pumping and vertical convection in the ocean. Thus warm and saline subsurface water may come in direct contact with the atmosphere. The heat loss to the atmosphere may then cool the water sufficiently that it sinks to intermediate depths. We therefore speculate that there is a link between the topographically induced atmospheric vorticity and the strong downstream cooling observed at 100–200 meters depth in the West Spitsbergen Current (Boyd and D'Asaro, 1994).

7. Acknowledgements

Discussions with Dr. M. A. Shapiro and Professor Elmer Raustein are appreciated. The super-computing time has been made available by The Norwegian Research Council.

REFERENCES

Baines, P. G. 1995. *Topographic effects in stratified flows*. Cambridge monographs on mechanics and applied mathematics, Cambridge University Press.

Boyd, T. J. and D'Asaro, E. A. 1994. Cooling of the West Spitsbergen Current: Wintertime Observations West of Svalbard. *J. Geophys. Res.-Oceans* **99** (C11), 22,597–22,618.

Davies, H. 1976. A lateral boundary formulation for multilevel prediction models. *Quart. J. R. Met. Soc.* **102**, 405–418.

Eliassen, A. and Palm, E. 1960. On the transfer of energy in stationary mountain waves. *Geofys. Publ.* **22**, 1–23.

Grønås, S., Foss, A. and Lystad, M. 1987. Numerical simulations on polar laws in the Norwegian Sea. *Tellus* **39A**, 334–353.

Grønås, S. and Hellevik, O. 1982. *A limited area prediction model at the Norwegian Meteorological Institute*. Technical Report 61, Det Norske Meteorologiske Institutt.

Haltiner, G. and Williams, R. 1980. *Numerical prediction and dynamic meteorology*. John Wiley & Sons, NY, 2nd edition.

Hanssen-Bauer, I., Kristensen Solås, M. and Steffensen, E. 1990. *The climate of Spitsbergen, KLIMA* 16. Det Norske Meteorologiske Institutt.

Jones, P. 1987. The twentieth century Arctic High. Fact or fiction? *Clim. Dyn.* **1**, 63–75.

Lindzen, R. 1981. Turbulence and stress due to gravity wave and tidal breakdown. *J. Geophys. Res.* **86**, 9707–9714.

Lott, F. and Miller, M. 1997. A new subgrid-scale orographic drag parameterization: Its formulation and testing. *Quart. J. R. Met. Soc.* **123**, 101–127.

Louis, J. 1979. A parametric model of vertical eddy fluxes in the atmosphere. *Boundary-Layer Meteorol.* **17**, 187–202.

Nordeng, T. 1986. *Parameterization of physical processes in a 3-dimensional numerical prediction model.* Technical report 65. Norwegian Meteorological Institute, Oslo, Norway.

Olafsson, H. and Bougeault, P. 1996. Nonlinear flow past an elliptic mountain ridge. *J. Atmos. Sci.* **53**, 2465–2489.

Overland, J. E. and Pease, C. H. 1982. Cyclonic climatology of the Bering Sea and its relation to sea ice extent. *Mon. Wea. Rev.* **110**, 5–13.

Pedlosky, J. 1979. *Geophysical fluid dynamics.* Springer Verlag, New York.

Peltier, W. and Clark, T. 1979. The evolution and stability of finite amplitude mountain waves. Part II: Surface wave drag and severe downslope windstorms. *J. Atmos. Sci.* **36**, 1498–1529.

Quadfasel, D., Rudels, B. and Kurz, K. 1988. Outflow of dense water from a Svalbard fjord into the Fram Strait. *Deep Sea Research* **35**(7), 1143–1150.

Schär, C. and Smith, R. 1993. Shallow-water flow past isolated topography, I: Vorticity production and wake formation. *J. Atmos. Sci.* **50**, 1373–1400.

Schauer, U. 1995. The release of brine-enriched shelf water from Storfjord into the Norwegian Sea. *J. Geophys. Res.-Oceans* **100**, 16,015–16,028.

Serreze, M., Box, J., Barry, R. and Walsh, J. 1993. Characteristics of arctic synoptic activity, 1952–1989. *Meteorology and Atmospheric Physics* **51**, 147–164.

Serreze, M., Kahl, J. and Schnell, R. 1992. Low-level temperature inversions of the Eurasian arctic and comparisons with Soviet drifting station data. *J. Climate* **5**, 615–629.

Smith, R. 1985. On severe downslope winds. *J. Atmos. Sci.* **42**, 2597–2603.

Smith, R. 1989a. Hydrostatic airflow over mountains. In: *Advances in geophysics.* Academic Press Inc.

Smith, R. 1989b. Mountain-induced stagnation points in hydrostatic flow. *Tellus* **41A**, 270–274.

Smith, R. and Grønås, S. 1993. Stagnation points and bifurcation in 3-D mountain airflow. *Tellus* **45A**, 28–43.

Smolarkiewicz, P. and Rotunno, R. 1989. Low Froude number flow past three-dimensional obstacles. Part I: Baroclinically generated lee vortices. *J. Atmos. Sci.* **45A**, 28–43.